A cascade thermoacoustic engine

D. L. Gardner and G. W. Swift[a)]
Condensed Matter and Thermal Physics Group, Los Alamos National Laboratory, Los Alamos, New Mexico 87545

(Received 11 April 2003; revised 29 July 2003; accepted 4 August 2003)

A cascade thermoacoustic engine is described, consisting of one standing-wave stage plus two traveling-wave stages in series. Most of the acoustic power is produced in the efficient traveling-wave stages. The straight-line series configuration is easy to build and allows no Gedeon streaming. The engine delivers up to 2 kW of acoustic power, with an efficiency (the ratio of acoustic power to heater power) of up to 20%. An understanding of the pressure and volume-velocity waves is very good. The agreement between measured and calculated powers and temperatures is reasonable. Some of the measured thermal power that cannot be accounted for by calculation can be attributed to Rayleigh streaming in the two thermal buffer tubes with the largest aspect ratios. A straightforward extension of this work should yield cascade thermoacoustic engines with efficiencies of around 35–40% of the Carnot efficiency. © *2003 Acoustical Society of America.* [DOI: 10.1121/1.1612483]

PACS numbers: 43.35.Ud, 43.25.Vt [RR]

I. INTRODUCTION

Rayleigh's criterion[1] for self-sustained heat-driven acoustic oscillations, ''If heat be given to the air at the moment of greatest condensation or be taken from it at the moment of greatest rarefaction, the vibration is encouraged,'' is the foundation of the many thermoacoustic schemes for producing acoustic power from heat without moving parts. Early concepts include the heat-driven electric generators described by Marrison,[2] Carter and Feldman,[3,4] and Ceperley.[5,6] Marrison's engine used standing-wave phasing and deliberately imperfect thermal contact to achieve Rayleigh's criterion, and had mature heat exchangers but without anything like today's stack between them.[7] The engines of Carter, Feldman *et al.* also used standing-wave phasing and deliberately imperfect thermal contact, and had stacks but no mature heat exchangers. Taking a completely different approach, Ceperley realized that Stirling engines[8] had always been meeting Rayleigh's criterion, using traveling-wave phasing and excellent thermal contact in a regenerator surrounded by mature heat exchangers, so he suggested acoustic networks to eliminate the Stirling engines' pistons.

Thermoacoustic research has progressed steadily over succeeding decades, and profited greatly from the publication of Rott's mathematical treatment.[9–11] A wide variety of standing-wave engines,[12–15] as illustrated in Fig. 1(a), has been built combining practical aspects of Marrison's and Feldman's work and based on Rott's theory. More recently, traveling-wave engines with the toroidal topology suggested by Ceperley, shown in Fig. 1(b), have also been demonstrated.[16–18] However, efforts to commercialize such engines have not yet succeeded.

The straight-line, closed–open topology shown in Fig. 1(a) works because the imperfect thermal contact in a stack can meet Rayleigh's criterion for acoustic-power production using pressure–velocity phase differences anywhere near that of a standing wave.[19] Acoustic power can flow out of both ends of the stack, mostly at the ambient end as in Fig. 1(a) or mostly at the hot end.[20,21] Although this straight-line topology is the simplest to build, the deliberately imperfect thermal contact on which it relies limits its efficiency.[19] The best traveling-wave engines[17,22] (and traditional Stirling engines) have 50% higher efficiency than the best standing-wave engines because the thermal contact in regenerators is excellent. However, they require phasing near that of a traveling wave to create acoustic power: Traveling-wave engines only amplify, so power can only flow out of the hot end of a regenerator if a smaller power is fed into the ambient end.[19,23] The toroidal topology shown in Fig. 1(b) achieves this by feeding some of the engine's own power, from the regenerator's hot end, back to its ambient end. Unfortunately, the toroidal topology is more difficult to build than the straight-line topology, and also suffers from a circulating second-order mass flow, Gedeon streaming,[24] that can reduce or eliminate the efficiency advantage by convecting heat from the hot heat exchanger to one of the ambient heat exchangers. Gedeon streaming has been successfully suppressed by exploiting the time-averaged pressure gradient developed in oscillating flow through an asymmetric channel,[17] but this consumes acoustic power. In addition, fabricating asymmetric channels that are adjustable, to stop Gedeon streaming under a variety of operating conditions, adds complexity that is undesirable in commercial devices.

In this paper we describe our first attempt to enjoy the best features of standing-wave engines and traveling-wave engines simultaneously, by arranging a standing-wave engine and one or more traveling-wave engines in a series, as shown in Fig. 1(c), a topology we call a ''cascade.'' The straight-line topology is easy to build, automatically prevents Gedeon streaming, and has high velocities only where streamlining is easy, while the efficiency is reasonably high because most of the acoustic power can be created in the traveling-wave stage or stages.

a)Electronic mail: swift@lanl.gov; URL: www.lanl.gov/thermoacoustics/

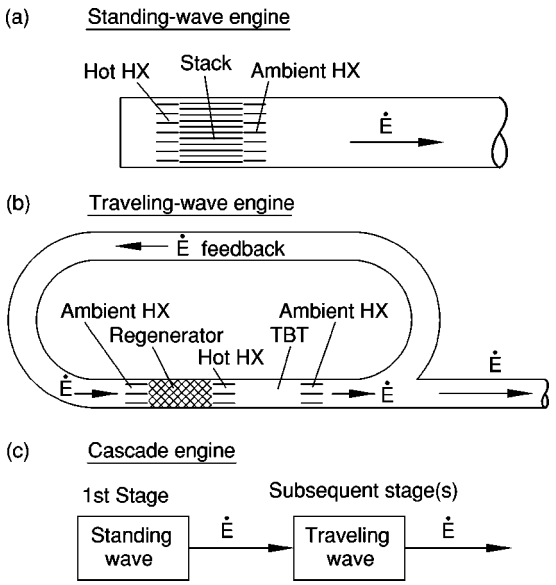

FIG. 1. Some thermoacoustic engine topologies. HX=heat exchanger, TBT=thermal buffer tube, $\dot{E}$=acoustic power. (a) In a standing-wave engine, the temperature difference between the hot heat exchanger and the ambient heat exchanger falls across the stack, whose pore dimensions are of the order of a few thermal penetration depths. Here, the standing-wave engine is in a simple cylindrical resonator, closed at its hot end and delivering acoustic power through its ambient end. (b) In a traveling-wave engine, the temperature difference between the hot heat exchanger and the ambient heat exchanger falls across the regenerator, whose pore dimensions are much smaller than a thermal penetration depth. Acoustic power can only be produced if some is fed into the ambient end of the regenerator, such as through the acoustic feedback path shown here. (c) The cascade engine combines one standing-wave engine with one or more traveling-wave engines. The standing-wave engine supplies the acoustic power needed at the ambient end of the adjacent traveling-wave engine.

Much of our fundamental thermoacoustics work at Los Alamos is motivated by our collaboration with Praxair, Inc., directed toward the development of powerful thermoacoustic natural-gas liquefiers.[25] Hence, we decided to build a cascade engine that might provide guidance to some future aspect of that collaboration, while still at low enough power for convenient laboratory experimentation. The experimental engine is ''similar'' to a hypothetical 35-kW engine. Similitude[26] in thermoacoustics shows that reducing all dimensions of such a hypothetical engine by a factor of two and changing from helium to argon (at a slightly lower pressure) preserves all dimensionless thermoacoustic variables such as Mach numbers, Reynolds numbers, and ratios of penetration depths to pore sizes. All thermoacoustic behavior, both linear and nonlinear, is identical when expressed with dimensionless variables. This scaling lets the experimental engine fit vertically in our lab and reduces the total heater power required so that electric heaters easily suffice.

In Sec. II we summarize the qualitative considerations that led us to adopt this particular cascade configuration: one standing-wave stage and two traveling-wave stages located within one pressure maximum of the wave. In Sec. III we describe the construction of this apparatus. The principal complexity was the need to design and build about three times more parts than for previous thermoacoustic engines, due to the presence of three stages. This complexity is reflected throughout the paper, as there are three sets of parts to describe, often three sets of data to explain, and many references to cite. In Sec. IV we describe the initial debugging, measurements of heat leak, and the evolution of the thermoacoustic measurements, as some problems were solved while others grew. In Secs. V and VI we describe the thermoacoustic measurements in detail, with pressure and volume–velocity waves in Sec. V and temperatures and powers in Sec. VI. Our understanding of the waves is very good, but an understanding of the powers leaves room for future work, including the study of heat transport by streaming in thermal buffer tubes. Finally, in Sec. VII we discuss the efficiency of the cascade. Although this engine converted heater power to acoustic power with an efficiency of only 20%, many of the sources of inefficiency are due to our decision to build a similitude scale model, and others are probably associated with one design error discussed below. We are confident that cascade engines can be built with efficiencies in the range of 35%–40% of Carnot's efficiency, the upper end of this range equaling the highest measured efficiency in a thermoacoustic engine to date.[17]

II. BROAD DESIGN CONSIDERATIONS

To design an experimental test of the cascade idea, we began with decisions about the number of stages and the resonator type, guided by the qualitative and approximate considerations (principally of efficiency and size) described in this section. After these decisions were made, we relied on a numerical analysis to select specific dimensions and other details, compromising as necessary to satisfy practical fabrication constraints.

The number of stages is an important issue. A traveling-wave stage can create acoustic power from thermal power with high efficiency, but, in the linear topology of the cascade shown in Fig. 1(c), the traveling-wave stage must be supplied with acoustic power from another stage, such as a standing-wave stage. If τ is the ratio of hot and ambient (absolute) temperatures, the acoustic-power gain[5] of a traveling-wave stage is approximately τ and the acoustic power created in it is approximately proportional to $\tau-1$. Then a series combination of a standing-wave stage with efficiency of $\sim 1/5$ and $N-1$ traveling-wave stages each with efficiency $\sim 1/3$ has an overall efficiency,

$$\eta \sim \frac{\tau^N}{2+3\tau^N}, \tag{1}$$

showing how the efficiency grows with the number of stages, as more and more acoustic power is created in the efficient traveling-wave stages: $\eta=0.20$ for one stage (standing-wave only), $\eta=0.26$ for two stages and $\tau=2.5$, $\eta=0.30$ for three stages and $\tau=2.5$, $\eta=0.32$ for four stages and $\tau=2.5$, and $\eta=0.33$ for an infinite number of stages. Hence, three or four stages seems to be an acceptable compromise between the optimum efficiency of a large number of stages and the simplicity of a small number of stages.

Ceperley[5] realized that the best efficiency in traveling-wave engines is obtained when the time phase ϕ by which oscillating pressure p_1 leads oscillating velocity u_1 is near zero. Figures 2(a)–(d) show four ways to satisfy this crite-

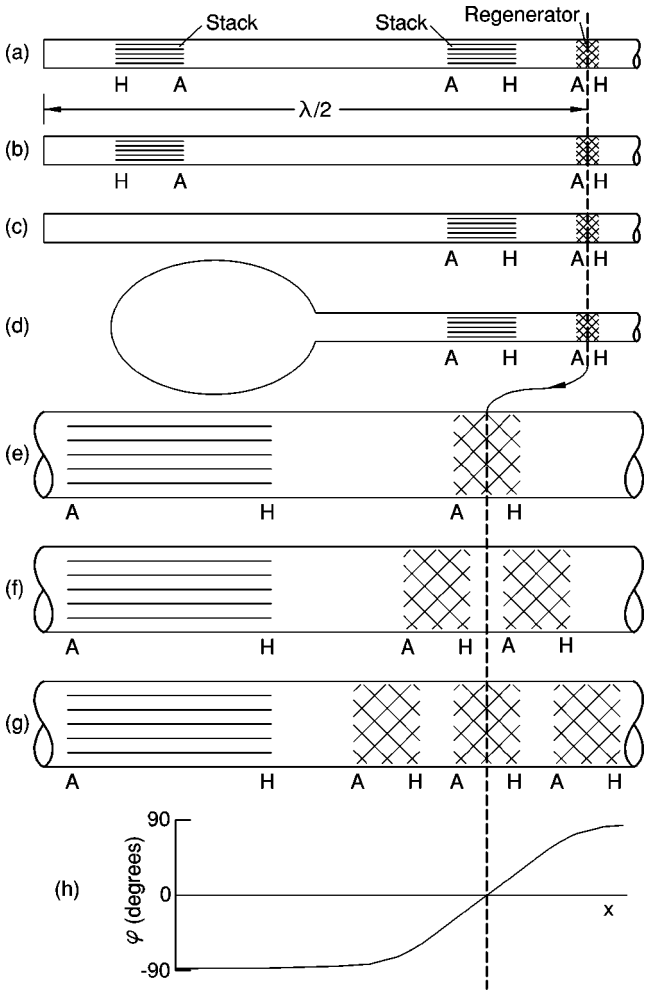

FIG. 2. An illustration of some alternatives in the design of cascade engines. The dashed line running through all parts of the figure marks the location of the sweet spot where the phase ϕ by which pressure leads velocity is zero. Acoustic power flows out of the right end of the apparatus in all cases. H and A indicate the hot and ambient ends, respectively, of each stack or regenerator. For clarity, heat exchangers and thermal buffer tubes are not shown. Parts (a) through (d) illustrate options for the resonator and the standing-wave stage(s); we chose (d). Parts (e) through (g) illustrate a closer view of different numbers of traveling-wave stages; we chose (f). Part (h) illustrates ϕ as a function of position in (e) through (g).

rion: with a traveling-wave stage at the ''sweet spot'' of zero phase, fed by one or two standing-wave stages. From these, we chose (d) to keep the total height of the apparatus as short as possible; other criteria (such as minimum weight) might encourage a different choice.

Ceperley[6] also realized that the magnitude of the specific acoustic impedance z of a pure traveling wave is too low for efficient traveling-wave engine performance, because the relatively high velocity present in a pure traveling wave causes high viscous dissipation of acoustic power in the regenerator and high shuttle transport of heat through the regenerator. The best performance requires $|z| \sim 10\rho_m a$, where ρ_m is mean density and a is sound speed. Initially, we simply assumed that we would be able to reach such a condition in the traveling-wave stages by changing area from stage to stage (not shown in Fig. 2); later detailed design calculations confirmed this assumption.

Another factor affecting efficiency is the number of traveling-wave stages that can be collocated at the sweet spot of zero phase, as illustrated in Figs. 2(e)–(h). When $|z| \gg \rho_m a$, the sweet spot is a significant local minimum in velocity. Viscous dissipation of acoustic power in a regenerator and heat transport through a regenerator due to imperfect thermal contact are both proportional to $|u_1|^2$, so a doubling of $|u_1|^2$ from its minimum value at the sweet spot can be taken as a rough measure of how far from the sweet spot a regenerator might acceptably be. Moving away from the sweet spot, the volume velocity U_1 grows according to the continuity equation,[27]

$$\frac{dU_1}{dx} \sim -i\omega c p_1, \tag{2}$$

where ω is the angular frequency, c is the compliance per unit length, $i = \sqrt{-1}$, and the subscript 1 denotes a complex variable. With changes in U_1 90° out of phase from U_1 itself, a doubling of $|U_1|^2$ occurs when $\phi \sim 45°$. Hence, multiple traveling-wave stages should be crowded together within $\phi \sim \pm 45°$ of the sweet spot. However, a thermal buffer tube is needed between stages to insulate the ambient end of one stage from the hot end of its neighbor. For effective insulation, the length L_{tbt} of a thermal buffer tube must be of the order of 10 times the gas displacement amplitude $|u_1|/\omega$. Combining this requirement with $|z| \sim 10\rho_m a$ yields

$$L_{\mathrm{tbt}} \sim 10|u_1|/\omega \sim |p_1|/\omega\rho_m a \sim \lambda/100, \tag{3}$$

for $|p_1|/p_m \sim 0.1$, where λ is the acoustic wavelength. Taking $L_{\mathrm{tbt}}/\gamma p_m$ as the minimum compliance per unit area between stages, Eqs. (2) and (3) show that $\Delta|U_1| \sim |U_1|$. Hence, for $|p_1|/p_m \sim 0.1$, the practical limit is two or possibly three traveling-wave stages in one pressure maximum. The heat exchangers and the regenerator itself have compliance in addition to that of the thermal buffer tube, so it seems unlikely that more than two traveling-wave stages can effectively share one sweet spot.

Hence, we chose a combination of Figs. 2(d) and (f) for our apparatus.

III. APPARATUS

The cascade apparatus, shown in Fig. 3, has its three engine stages in the center of a tall, thin resonator with a single pressure antinode in the center. It was built of welded steel, mostly 304 and 316 stainless steel for strength at high temperatures and rust resistance in water-cooled heat exchangers, but with carbon steel for some parts of the pressure vessel. The wall thicknesses of all pressure barriers were determined using Sec. VIII of the Pressure Vessel Code.[28] Two flanged rubber-O-ring seals, shown as collars just above and below the pressure housing in Fig. 3, enable handling the apparatus in three parts of roughly equal height. In the following top-to-bottom description of the apparatus, lengths reported are along the acoustic axis (generally vertical) and diameters reported are inside diameters.

Above the 1st stage, the upper portion of the resonator, which is of the type shown in Fig. 2(d), was designed for the minimum dissipation of acoustic power without regard for size. The 1.0-m long compliance at the top has a volume of

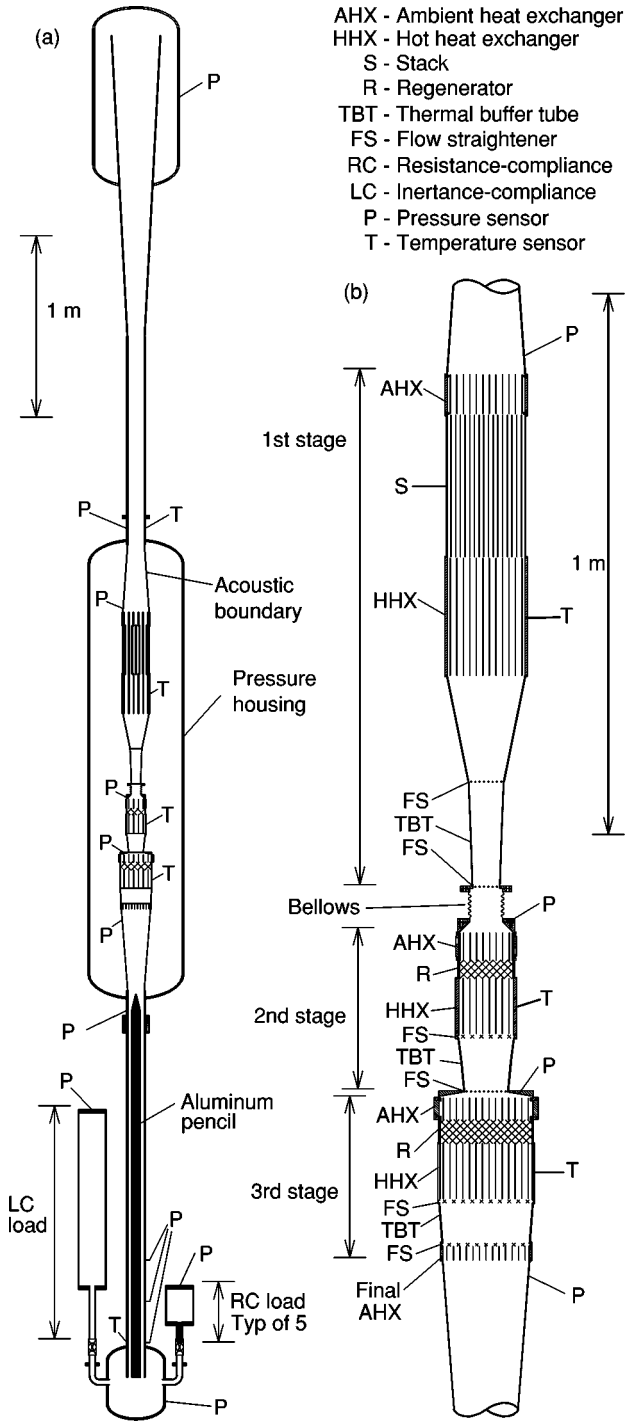

FIG. 3. The cascade engine built for this work. Everything is drawn to scale except the pores inside the heat exchangers, stack, regenerators, and flow straighteners. (a) The entire system, including (from top to bottom) the upper resonator, the cascade engine inside the pressure housing, and the lower resonator and load components. (b) A more detailed view of the three stages in the cascade engine. The 1st stage is a standing-wave engine; the 2nd and 3rd stages are traveling-wave engines. The major components and sensors are identified by the legend in the figure.

$0.11\ m^3$ outside the conical penetration in it. This cone is 1.66-m long and penetrates 0.83 m into the compliance, ending there with an inside diameter of 0.26 m. The cone lowers the acoustic velocity of the gas entering the compliance, reducing minor-loss dissipation of acoustic power there, and its penetration far into the compliance keeps the overall height of the apparatus (7.8 m) as short as possible. The small diameter of the cone smoothly joins the 9.0-cm-diam, 1.14-m long upper resonator pipe that penetrates the pressure housing. A flowing-water jacket (not shown in Fig. 3) surrounds most of the exposed portions of this pipe and half of the cone above it, but there was so little dissipation of acoustic power in the upper portion of the resonator that shutting off its water made no noticeable difference to the engine's performance. A 0.38-m long cone connects the lower end of the resonator pipe smoothly to the 1st-stage ambient heat exchanger.

The pressure housing surrounding the three stages contains the 2.4-MPa mean argon pressure, so that the inner shells labeled an ''acoustic boundary'' in Fig. 3(a) need to support only the acoustic pressure amplitude. Thus, the walls of this acoustic boundary around the stack, regenerators, and thermal buffer tubes are only 1–2 mm thick (depending on diameter and temperature), much thinner than would be required if they supported the mean pressure, with a concomitant reduction of heat leaks. The space between the acoustic boundary and the pressure housing was packed with refractory ceramic fiber thermal insulation,[29] to a density of $10\ lb/ft^3$, to reduce heat leak from the hot heat exchangers. Despite this dense packing of the insulation, the argon permeating it experienced significant gravity-driven convection, which is discussed in the next section.

Most of the quantitative details of the construction of the three stages of the cascade engine are presented in Table I. The uppermost component, the 1st-stage ambient heat exchanger, is of traditional, welded tube-and-shell design, with the argon oscillating vertically through the tubes and ambient-temperature water flowing crosswise in the spaces between the tubes. The water is delivered through three 10-mm-diam ports on one side, and removed similarly from the other side. Below this heat exchanger is a honeycomb stack[30] with 1 mm between opposite flats in each hexagonal channel in the honeycomb. Next comes the electrically heated 1st-stage hot heat exchanger, consisting of a cross-drilled stainless-steel cylinder. The oscillating argon passes through the axial holes, and the 6.4-mm-diam transverse holes hold electric cartridge heaters of various lengths corresponding to the hole lengths. The heaters are wired in three parallel groups in a Delta configuration and supplied with three-phase 60-Hz power through three mechanically linked variable autotransformers connected to the 208-Volt mains.

The taper angle of the 1st-stage thermal buffer tube was designed to suppress Rayleigh streaming,[31] and the stainless-steel-screen flow straighteners at the ends of the thermal buffer tube were designed to prevent jet-driven streaming.[19] Together, these features were intended to encourage thermally stratified oscillating flow in the thermal buffer tube, without gross convection of heat from hot to ambient. A 0.20-m long ''hot cone'' connects the bottom of the 1st-stage hot heat exchanger to the top of the 1st-stage thermal buffer tube. Without the hot cone, the velocity at the top of the 1st-stage thermal buffer tube would have been too high to preserve laminar flow in the boundary layer, and the taper angle calculated to suppress Rayleigh streaming in this ther-

TABLE I. Dimensions and other details of the three stages of the cascade. HX = heat exchanger, TBT = thermal buffer tube. Ranges of diameters for thermal buffer tubes indicate a conical taper. Gaps of 2–3 mm at interfaces between components are not tabulated.

	Length (cm)	Diam (cm)	Porosity	Number of bores on axis	Bore diam (mm)	Number of heaters	Mesh (wires/inch)	Wire diam (μm)	Number of screens
1st stage									
Ambient HX	7.62	14.3	43%	283	5.54				
Stack	26.0	14.3	92%	~20,000	0.97				
Hot HX	21.5	14.3	17%	88	6.35	108			
Flow str.		6.39					16	410	2
TBT	19.4	6.39–4.94							
Flow str.		4.94					16	410	1
2nd stage									
Ambient HX	5.40	10.1	20%	361	2.36				
Regenerator	3.10	10.1	75%				145	56	278
Hot HX	10.2	10.1	12%	124	3.18	54			
Flow str.		10.1					50	190	13
TBT	9.90	10.1–7.92							
Flow str.		7.92					50	140	1
3rd stage									
Ambient HX	4.30	17.1	20%	1139	2.36				
Regen. (1st half)	2.05	17.1	75%				180	46	224
Regen. (2nd half)	2.15	17.1	76%				120	66	155
Hot HX	10.2	17.1	12%	362	3.18	78			
Flow str.		17.1					50	190	13
TBT	7.50	17.1–16.0							
Flow str.		16.0					50	190	13
Final amb. HX	2.54		20%	913	2.36				

mal buffer tube would have been too steep to prevent flow separation.

The small end of the 1st-stage thermal buffer tube is bolted and sealed to a ten-convolution, 8-cm long flanged bellows having diameter 4.9 cm, which accommodates thermal expansion of the three heated engine stages relative to the pressure housing. Below, the bellows connects to a 2-cm long transition cone, which, in turn, connects to the 2nd stage.

The 2nd and 3rd stages are similar in character to the 1st, with tube-and-shell ambient heat exchangers, electrically heated hot exchangers, and tapered thermal buffer tubes between stainless-steel-screen flow straighteners. In place of the honeycomb stack of the 1st stage, the 2nd and 3rd stages have regenerators made of stacked circular pieces of stainless-steel screen. The velocities at the transitions from the hot heat exchangers to the thermal buffer tubes are low enough in these stages that nothing like the hot cone of the 1st stage is needed. A 1.2-cm long transition cone accommodates the diameter mismatch between the bottom of the 2nd stage and the top of the 3rd stage.

A 0.45-m long cone reaches from the final ambient heat exchanger to the 2.13-m long, 9.0-cm-diam lower resonator pipe exiting the pressure housing and penetrating 16 cm into the lower compliance. A flowing-water jacket (not shown in Fig. 3) surrounds most of the exposed portion of this pipe above the pressure transducers, and dissipation of acoustic power in this part of the apparatus was high enough that shutting off the flowing water endangered the transducers. An error in the initial design of the apparatus, described in the next section, required a large increase of inertance in the lower resonator pipe after the apparatus was built. This was accomplished by retrofitting a 2.11-m long, 5.1-cm-diam aluminum ''pencil'' [shown in Fig. 3(a)], streamlined at its upper end, into the lower resonator pipe, to reduce the pipe's area.

The lower compliance, which has a volume of 0.024 m^3, has six penetrations leading through six ball valves to five RC loads and one LC load, to consume power from the engine and to change the phase of the impedance of the lower resonator, respectively. The resistive element ''R'' in each RC load is a 10-cm long brass cylinder having diameter 3.3 cm and drilled axially with nineteen 2.4-mm holes, providing a resistance of 6 MPa s/m^3 at a typical operating amplitude. The 3.0-liter compliance volume ''C'' of each RC load was chosen to cancel the inertial impedance of its penetration, connecting piping, and ball valve so that the impedance of each RC load was real. The 16-liter compliance volume of the LC load was chosen to make its compliant impedance much smaller than the inertial impedance of its penetration, connecting piping, and ball valve, and no deliberate resistive component was present, so that this load was as inertial as possible. The inertial parts of the LC load have a total length of 41 cm and a diameter of 2.5 cm, resulting in an inertial impedance of 5 MPa s/m^3. (However, the resistive impedance due to turbulence in these parts was not insignificant.)

Piezoresistive pressure transducers[32] at the locations shown in Fig. 3, sensed with a lock-in amplifier, were used to measure oscillating pressure amplitudes and phases. The four pressure transducers inside the pressure housing measured the pressure differences between the cascade and the pres-

sure housing, while the others measured the differences between the apparatus and atmospheric pressure. Sheathed, ungrounded, type-K thermocouples were used to measure temperature. Temperatures of metal parts in the cascade, where shown in Fig. 3, were measured with thermocouples inserted into short, close-fitting tubes that had been tack welded to the metal parts, and these were recorded with a personal computer. In hindsight, we should have ensured better thermal contact between these thermocouples and their metal parts, because heat carried to them through the fiber-insulation space, either by conduction or convection, was often noticeable. The temperatures of water streams flowing into and out of each heat exchanger were measured with thermocouples inserted into the flowing streams, not shown in Fig. 3, and these were sensed with a hand-held digital readout. Rotameters on each water stream sensed the flow rates, and together with the density and specific heat of water these yielded the measured heat-rejection powers removed from the engine at the four ambient heat exchangers. Electric powers to the three hot heat exchangers were measured with commercial electronic power meters.[33]

IV. DESCRIPTION AND HISTORY OF THE MEASUREMENTS

Measurements unfolded in the course of several episodes, with unforeseen problems occurring and evolving from episode to episode.

Initially, heating the three hot heat exchangers to 500 °C produced no oscillations at all, even though we expected the oscillations to appear below 400 °C. An analysis of this disheartening situation revealed a serious design error: The volume of the bottom compliance was half of what it should have been, distorting the wave so badly that the phase of U_1 in the middle of the apparatus would differ from what was intended by as much as 70°. The constraints of the floor-to-ceiling height of the room and the width of the system's support frame discouraged making a new, larger compliance, so the inertance of the lower resonator pipe was increased by insertion of the 2.11-m long pencil described above. An analysis showed that this retrofit would re-shape the expected wave well enough to make the engine work, though not optimally: It increased the dissipation of acoustic power by increasing both the overall surface area of the lower resonator tube and the velocity in it at a given pressure amplitude in the engine. Accordingly, this would not be a good design for efficiently delivering acoustic power to an external load. The retrofit was adequate to bring the acoustic impedances in the 2nd- and 3rd-stage regenerators near their design values. Streaming in the thermal buffer tubes is especially sensitive to impedance, and the retrofit left the 3rd-stage thermal-buffer-tube impedance significantly different than its optimum, as is discussed in Sec. VI.

Following insertion of the pencil, heating the hot heat exchangers to 600 °C still produced no oscillations. One thermometer at the axial center of the 1st-stage stack's shell indicated a temperature near 550 °C, suggesting that strong gravity-driven convection might be occurring in the stack. The dimensionless number governing such convection, the Grashof number $\rho_m^2 G\beta(T_{\text{hot}}-T_{\text{ambient}})hr_h^2/\mu^2$, where β and μ are the thermal-expansion coefficient and viscosity of the gas, G is the acceleration of gravity, T is temperature, h is the height of the stack, and r_h is the hydraulic radius of its pores, is not one of the similitude-conserved thermoacoustic numbers; G was not included in the similitude analysis of Ref. 26. The Grashof number in the argon in this stack was 6 times larger than it would be in the stack of the hypothetical 35-kW helium engine, to which this engine is otherwise similar. Hence, this gravity-driven convection was an unfortunate consequence of our decision to build an argon "scale-model" engine. Fortunately, lowering the mean pressure by only 30% reduced ρ_m and the strength of the convection enough to let the acoustic oscillations begin, near 25 Hz as expected. The strong tendency of the acoustic oscillations to maintain an energy-conserving, nearly linear temperature profile in the stack (expressed by the presence of the axial mean temperature gradient dT_m/dx in the thermoacoustic energy equation[10,19]) then stabilized the 1st stage against gravity-driven convection as the mean pressure was returned to its design value. We followed this awkward but reliable startup procedure at the beginning of each day of measurements.

TABLE II. Values of the constants A and B appearing in Eq. (4).

	A (W/K)	B (W)
1st ambient HX	0.15	0
1st hot HX	0.24	10
2nd ambient HX	0.40	10
2nd hot HX	0.33	30
3rd ambient HX	0.52	30
3rd hot HX	0.44	100
Final ambient HX	0	100

Measurements of heat leaks with no acoustic oscillations showed that the 2nd- and 3rd-stage heat leaks increased only about 30% when the argon mean pressure was raised from 0.1 to 2.3 MPa, while the 1st-stage heat leak increased tenfold over the same pressure range, confirming the presence of strong convection in the 1st stage. We did not study this carefully, because we saw no way to distinguish experimentally between convection in the stack and regenerators and convection in the pressurized fiber-packed insulation space around the outsides of the stack and regenerators. Using the density and viscosity of argon and the porosity and average fiber size of the insulation, we crudely estimated that convection in the insulation space might carry three times more heat leak than conduction in it. This supported the observation that almost all of the power applied to each hot heat exchanger during heat-leak measurements appeared at the ambient heat exchanger above it, and that the outside of the pressure vessel felt cool, except near the 1st stage. From these measurements, we arrived at a rough estimate of the heat leaks $\dot{Q}_{\text{leak}}$ that we added to the thermoacoustic calculations of thermal power at each heat exchanger:

$$\dot{Q}_{\text{leak}}=A(T_{\text{hot}}-T_{\text{ambient}})+B\frac{T_{\text{hot}}^4-T_{\text{ambient}}^4}{(900\ \text{K})^4}, \tag{4}$$

where T is absolute temperature and the values of A and B are given in Table II. At the highest operating temperatures,

these estimated heat leaks range from 100 W to 400 W, and probably have uncertainties of 100 to 200 W.

We first ran the engine with no RC loads to postpone the risky higher hot temperatures associated with higher powers as long as possible. During the measurements, we eventually noticed that the lower compliance (with its pressure transducer) became uncomfortably hot to the touch, so we installed a fan to blow room air on it.

Shortly after beginning to add loads to the engine, we noticed a time-dependent, weak resistance to ground in one pressure transducer, which is discussed in more detail in the next section. At about the same time, a small leak developed between the acoustic space and the fiber-insulation space. The first manifestation of this leak was a diode-like characteristic: a dc pressure difference of about 50 kPa between the two spaces whenever the acoustic oscillations were present. Most of the loaded data were obtained while this small leak was present. We did not notice the presence of this leak immediately, so many of the data sets were obtained at a mean pressure of 2.33 MPa, instead of 2.38 MPa used for most data before the leak appeared. Shortly after our first use of the LC load took the hot temperatures to new highs (660 °C on the hot cone in the 1st stage, 605 °C on the three hot heat exchangers), the leak increased quickly, and, fearing the intrusion of ceramic fiber insulation into the acoustic space, we ended the measurements. Earlier, repeated measurements at 10% amplitude, both with and without load, had been reproducible, suggesting that the appearance and initial evolution of this leak had not been affecting the thermoacoustic performance.

After all measurements were complete, disassembly revealed probable causes of these problems. First, we found about half a liter of water in the fiber-insulation space. There were no leaks from the ambient heat exchangers or their water pipes, so this water must have been present from the beginning. We surmise that the fiber insulation became damp when we stored it outdoors for a few months before assembling the engine. (The insulation packaging had been damaged; we would not have noticed the dampness during the assembly of the engine because we always wore rubber gloves when handling the insulation.) Engine operation at high temperatures and for long times would have gradually redistributed the water, driving it toward cooler and lower locations. The pressure transducer that developed the time-dependent resistance to ground was the lowest and presumably coolest of the four pressure transducers in the insulation space, so we ascribe its failure to this water. In the future, we will gently warm and patiently evacuate all such fiber-insulation spaces. Second, we found that the leak between the acoustic space and the fiber-insulation space was due to two fatigue cracks in welds on the uppermost and lowermost cones of the acoustic boundary inside the fiber-insulation space. In hindsight we realized that these ambient-temperature cones required slightly greater thickness to reliably survive the oscillating pressure in them.

To obtain a set of data with the engine oscillating, we opened selected load valves as desired, adjusted the powers to the three hot heat exchangers by hand until the pressure amplitude was at a desired value and the three hot temperatures were within 10 °C of each other, and then waited to ensure that a steady state was actually achieved. A minor adjustment of the total argon content of the apparatus was usually necessary to keep the mean pressure at the desired value as temperatures evolved. After at least an hour of adjustment and waiting, complex pressure amplitudes, temperatures, electric heater powers, and water flow rates were recorded, forming one steady-state data set. Twenty such data sets were obtained at mean pressures between 2.32 and 2.45 MPa, and are reported in this paper.

To calculate values with which to compare the measurements, we modeled the apparatus, from the upper compliance through the three stages to the lower compliance, with DeltaE.[34] DeltaE numerically integrates the one-dimensional acoustic continuity, momentum, and (when appropriate) energy equations. It does so in a geometry defined by the user as a sequence of segments, such as ducts, cones, stacks, regenerators, and heat exchangers. Solutions to the appropriate 1-d equations are found for each segment, with acoustic pressures, acoustic volume velocities, and mean temperatures matched at the junctions between segments. In stacks, regenerators, and thermal buffer tubes, the energy equation is solved simultaneously with the momentum and continuity equations to find the temperature profile as well as the acoustic variables. The energy flow through such segments is determined by temperatures and/or heat flows at adjacent heat exchangers. The user can define the geometry of each segment and the global variables such as mean pressure. In general, a single pass of DeltaE's integration requires values for some variables that the user does not know, and yields values for some other variables that the user does know. Hence, a shooting method is used to accommodate these irregularities. The DeltaE model of this apparatus included rough estimates for minor losses at the locations of a dozen abrupt area changes, based on tables published by Idelchik[35] for steady flow. With one exception discussed in Sec. VI, the model is very insensitive to the exact values of these minor-loss coefficients. When load was applied at the bottom of the engine, each RC or LC load was modeled with a separate DeltaE file, and the resulting net load impedance was imposed on the DeltaE model for the whole engine. (For the RC loads, the individual DeltaE load models yielded powers differing by only 1% from the simplest lumped-RC expression,[36]

$$\dot{E} = \frac{\omega V_C}{2\gamma p_m} \mathrm{Im}[p_{1,\mathrm{in}} \tilde{p}_{1,C}], \tag{5}$$

where V is volume, γ is the ratio of specific heats, the tilde denotes complex conjugation, and the subscripts C and ''in'' refer to the compliance and the inlet to the flow resistance, respectively. However, the more extended LC load required a DeltaE model for acceptable accuracy.) For each data set, we forced the whole-engine DeltaE model to have the measured mean pressure, the measured complex pressure at the transducer between the 2nd and 3rd stages, the measured common water inlet temperature as DeltaE's ''metal'' temperature at all four ambient heat exchangers, and the measured temperatures of the upper and lower resonator tubes. We also forced the model to have a common ''metal'' temperature for all three hot temperatures, but we did not choose its value. Del-

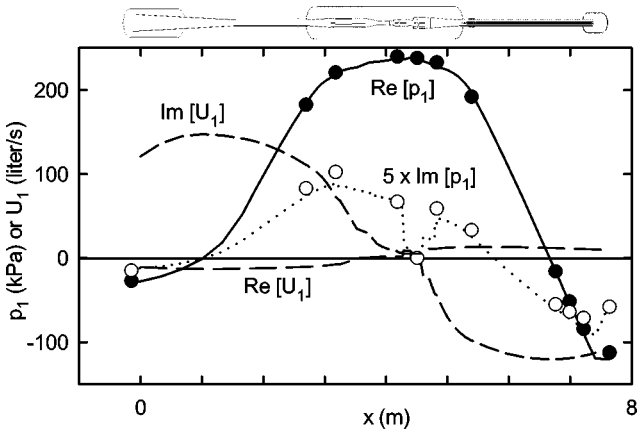

FIG. 4. Components of pressure and volume velocity for a typical operating point. Circles are measured values of the pressure, and lines are calculations. Re[ ] and Im[ ] denote real and imaginary parts. The calculated pressure is forced to agree with the measured pressure at $x=4.5$ m, where the phase is taken to be zero without loss of generality.

taE then computed as results the operating frequency, the wave profile throughout the apparatus, the common temperature of the three hot heat exchangers, and the thermal powers at the three hot heat exchangers and the four ambient heat exchangers.

For one of the data sets, we compared the calculated results for ''as-built'' dimensions and ''as-running'' dimensions, to learn whether thermal expansion of the hot parts and consequent compression of the bellows were significant. Differences were only of the order of 0.1% and 0.1°, so we performed all other calculations with as-built dimensions.

V. THE WAVE

We begin presentation of the data with the wave in the engine. Establishing agreement between the measured and calculated pressure phasors yields confidence in the calculated volume-velocity phasors, and together these two components of the wave form the basis for trying to understand the powers in the engine.

Figure 4 shows the components of the wave at 10% amplitude (i.e., $|p_1|/p_m=0.10$ at the pressure maximum between the 2nd and 3rd stages) with no RC or LC load applied to the bottom of the apparatus. Overall, the wave qualitatively resembles a half-wavelength standing wave, with its pressure maximum in the middle and volume-velocity maxima at the two ends. However, the compliances at the two ends have less than infinite volume, and the area of the intervening piping varies dramatically with x, so the actual wave is more intricately structured than the simple trigonometric functions associated with idealized geometries like those of Fig. 2. Note that the imaginary part of pressure is magnified $\times 5$ in the figure—like Re$[U_1]$, it is small enough to be unimportant for a qualitative overview of the standing wave.

The disagreements between measured and calculated complex pressures in Fig. 4 are typically 2%, and at most 6%, in amplitude, and typically 1°, and at most $3\frac{1}{2}$°, in phase. This accurate agreement between measurement and calculation is typical of all twenty data sets. The calculated frequency exceeded the measured frequency by 1.0% to 1.5% after the addition of the fan to cool the lower compliance (without the fan, the excess ranged from 0.6% to 1.6%), more evidence that the computer model describes the apparatus very well and that a more detailed discussion of the wave, presented next, is justified.

The thermoacoustic continuity equation,[27]

$$\frac{dU_1}{dx}=-i\omega c p_1-\frac{1}{r_\kappa}p_1+gU_1, \tag{6}$$

where $1/r_\kappa$ is the thermal-relaxation conductance per unit length and g is the complex gain constant, describes the changes in U_1 from place to place in the apparatus. Figure 5(a) shows the spatial distribution of the U_1 phasors throughout the three stages. Compared with this broad range of U_1 phasors, the p_1 phasors in this region are almost independent of position: 220 kPa at 5° above the 1st stage, 240 kPa at 3° between the 1st and 2nd stages, 280 kPa at 0° between the 2nd and 3rd stages, and 230 kPa at 3° below the 3rd stage. Hence, for a qualitative interpretation of Fig. 5(a) in terms of the continuity equation, the pressure phasors throughout all three stages can be taken to have essentially constant magnitude and zero phase.

The overall appearance of Fig. 5(a) shows Im$[U_1]$ varying smoothly from large and positive above the 1st stage to large and negative below the 3rd stage. This overall variation simply reflects the compressibility of the gas throughout the stages, appearing in the first term of Eq. (6). Meanwhile, Re$[U_1]$ varies from negative above the 1st stage to positive below the 3rd stage, as the acoustic power $\dot{E}=\frac{1}{2}\mathrm{Re}[p_1\tilde{U}_1]$ increases from a negative value to a positive value.

The 1st stage, with the largest volume of the three stages, has the largest compliance, and so it spans the largest range of Im$[U_1]$. In this stage, the increase in Re$[U_1]$ occurs in the stack, where the g term in Eq. (6), which contributes positively to Re$[U_1]$, dominates the r_κ term, which contributes negatively. The phase difference between U_1 and p_1 is approximately 90° in the stack, as it should be for a standing-wave engine.

The 2nd stage, with the smallest volume of the three stages, spans the smallest range in U_1. Across the regenerator, where $g\simeq(1/T_m)dT_m/dx$ is real, the third term in Eq. (6) by itself would cause a multiplication[5] of the magnitude of U_1 by $T_{\mathrm{hot}}/T_{\mathrm{ambient}}$, without a change in the phase of U_1. Since U_1 has a positive real component and p_1 is essentially constant, the acoustic power $\dot{E}$ is multiplied by the same factor, $T_{\mathrm{hot}}/T_{\mathrm{ambient}}$. The change in phase of U_1 in the regenerator is due to the first term in Eq. (6) and the compressibility of the gas in the regenerator. The 2nd-stage thermal buffer tube displays a significant change in Im$[U_1]$, because it has a significant volume.

Between the 2nd and 3rd stages, U_1 passes through the ''sweet spot'' where it has the same phase as p_1. This is the most efficient location for a regenerator; optimally, the two ends of the regenerator should straddle the sweet spot, as discussed in Sec. II. Large deviations from this condition cause the volume velocity through one or both ends the regenerator to be larger than it need be for the desired acoustic

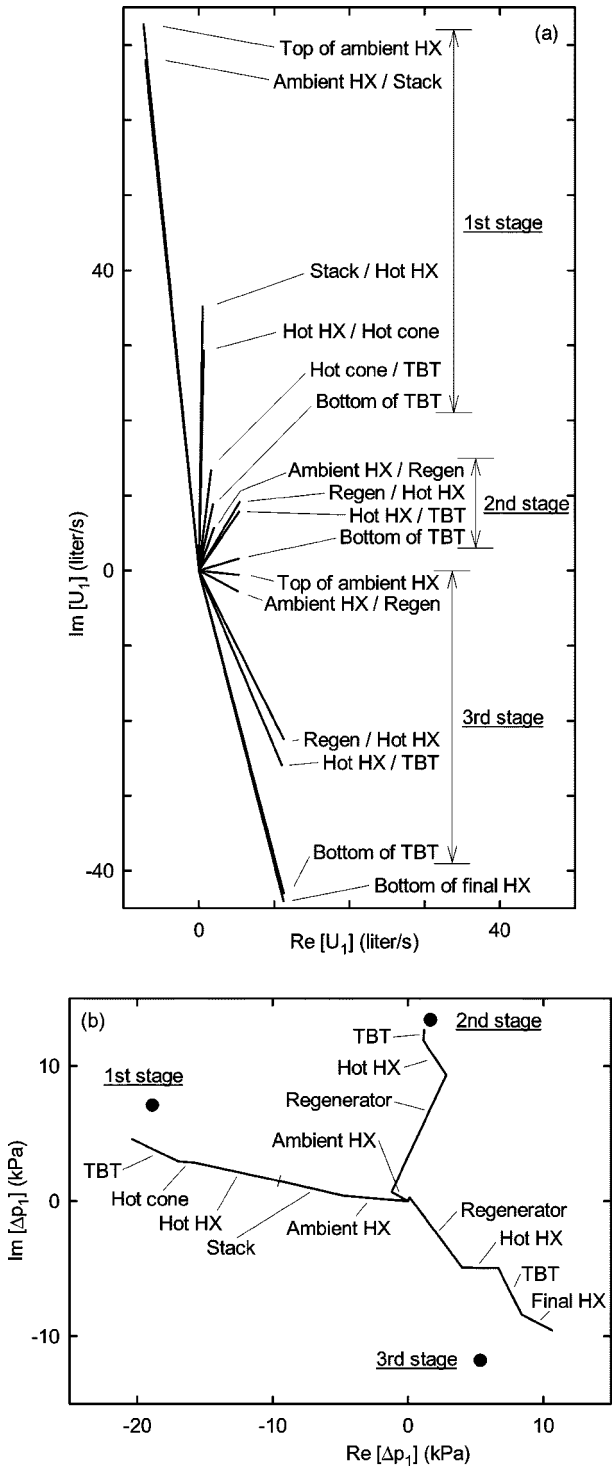

FIG. 5. Phasor diagrams for the operating point of Fig. 4. HX=heat exchanger; TBT=thermal buffer tube. As in Fig. 4, the zero of phase is chosen to be that of the pressure between the 2nd and 3rd stages. To avoid clutter, the conventional arrowheads have been omitted from the ends of the phasors. (a) Calculated volume-velocity phasors at several locations in all three stages. (b) Pressure-difference phasors for the same operating point. Circles are measured values, and lines are calculations showing how the total pressure-difference phasor across each stage is made up of smaller pressure differences across the components within that stage.

power, with attendant larger losses due to viscosity and imperfect thermal contact. The 2nd and 3rd stages in this apparatus are as close to the sweet spot as possible, given the requirement that the thermal buffer tube between them must have a volume significantly larger than the volumetric displacement within it. However, neither regenerator is actually close to traveling-wave phasing. (A calculation showed that the sweet spot was between the 1st and 2nd stages before retrofitting with the aluminum pencil discussed in previous sections.)

The U_1 phasors in the 3rd stage are similar to those of the 2nd, but with a different initial phase atop the ambient heat exchanger, and with larger changes from location to location, which reflect larger volumes in the 3rd stage. Again, across the regenerator, where $g \simeq (1/T_m)dT_m/dx$ is real, the third term in Eq. (6) by itself would cause a multiplication of the magnitude of U_1 by $T_{\text{hot}}/T_{\text{ambient}}$, without a change in the phase of U_1. Since U_1 has a positive real component, the acoustic power $\dot{E}$ is multiplied by the same factor. The accompanying change in phase of U_1 is due to the first term in Eq. (6) and the compressibility of the gas in the regenerator.

The thermoacoustic momentum equation,[37]

$$\frac{dp_1}{dx} = -i\omega l U_1 - r_\nu U_1, \tag{7}$$

where l is the inertance per unit length and r_ν is the viscous resistance per unit length, describes the changes in p_1 from place to place in the apparatus. The complex pressure throughout the three stages is so nearly spatially uniform that a pressure-phasor plot displays little detail. Hence, in Fig. 5(b) we display pressure *differences* across the stages and components. In the figure, the sign convention is chosen so that a resistive impedance creates a pressure-difference phasor in Fig. 5(b) that is parallel (not anti-parallel) with the corresponding volume-velocity phasor in Fig. 5(a). [This is opposite the sign convention of ordinary calculus, used in Eq. (7).] The three experimental points in Fig. 5(b) are differences between the complex pressures measured at the ends of each of the three stages, i.e., differences between adjacent pressure measurements at $x=3.2$, 4.2, 4.5, 4.8 m in Fig. 4. Each of the three corresponding calculated lines extending from the origin is a sequence of straight line segments, each of which shows the calculated pressure difference across a component within the stage. (Here, the thermal buffer tubes include the flow straighteners at their ends.) Hence, the three experimental points should lie close to the ends of the three lines.

This method of displaying the data accentuates experimental uncertainties, because the experimental points are small differences between large numbers. The uncertainty in the measured pressure phasors is about $1\frac{1}{2}\%$ in amplitude, i.e., 3 kPa, due to a combination of transducer calibration uncertainty, transducer-calibration temperature sensitivity, and lock-in gain uncertainty, so we expect the uncertainties in the differences $\text{Re}[\Delta p_1]$ shown in Fig. 5(b) to be a few kPa. The uncertainties in $\text{Im}[\Delta p_1]$ are smaller, about 1 kPa.

In the 1st stage, the net calculated pressure-difference phasor in Fig. 5(b) and all of its individual-component phasors lead the U_1 phasors of Fig. 5(a) by approximately 90°, indicating the mostly inertial nature of the impedance of this stage—each component within the 1st stage has much more

inertial impedance than resistive impedance. Additional resistance in the calculation of any one of the components within the 1st stage would rotate the corresponding straight line segment, and hence also the net Δp_1 phasor for the entire stage, clockwise toward the experimental point. For example, an additional resistance corresponding to 50 W of acoustic-power dissipation in the stack—only 10% of the power generated in the stack—would bring the calculated phasor into agreement with experiment. The validity of the ''tubular'' heat-exchanger algorithm used in DeltaE is doubtful at this level of accuracy, because it assumes laminar oscillatory flow while the Reynolds-number amplitude in the hot heat exchanger is 25,000 and in the ambient heat exchanger is 100,000. Furthermore, the applicability of the ''circular pore'' algorithm used in the DeltaE model for this hexagonal-honeycomb stack has never been checked to this level of accuracy. Hence, we believe that the small disagreement between the calculation and experiment in the 1st stage is probably due to the inaccuracy of one or both of these calculation algorithms.

The calculated 2nd-stage regenerator phasor in Fig. 5(b) is the largest segment of the net 2nd-stage Δp_1 phasor, and it points in a direction between those of the two U_1 phasors at the ends of the 2nd-stage regenerator in Fig. 5(a), indicating the resistive nature of the regenerator. The Δp_1 phasor segments for the 2nd-stage ambient and hot heat exchangers point somewhat counterclockwise from this direction, indicating the inertial contributions in these components. In the 2nd stage, the disagreement between the net calculated Δp_1 phasor and the experimental Δp_1 phasor is within the experimental uncertainty.

As in the 2nd stage, the regenerator in the 3rd stage makes the largest contribution to the 3rd-stage net Δp_1 phasor in Fig. 5(b). The impedances of the regenerator and of the thermal buffer tube are resistive, the latter because of its flow straighteners, its location where $|U_1|$ is high, and the low inertance of its large aspect ratio. The impedances of the 3rd-stage hot heat exchanger and final ambient heat exchanger have substantial inertial components, and the tiny pressure drop in the 3rd-stage ambient heat exchanger is barely visible in the figure.

The difference between the experimental and calculated 3rd-stage Δp_1 in Fig. 5(b) is difficult to explain. It is slightly larger than the expected experimental uncertainty of a few kPa, described above. To rotate the calculated net phasor to match the experimental phasor would require either elimination of all of the inertial impedance in the hot heat exchanger and final ambient heat exchanger, or a large clockwise rotation of most or all of the 3rd-stage U_1 phasors in Fig. 5(a); neither of these possibilities seems plausible. One possible explanation is that the pressure transducer at $x=4.8$ m, just below the final ambient heat exchanger, was already developing an electrical problem when this data set was taken. It is the one mentioned above that developed a time-dependent, weak resistance to ground, which we noticed later when experimentation with loads commenced. Thereafter it deteriorated erratically with time and experienced a change in ac sensitivity of several percent even when it was powered by a floating power supply and detected with a differential amplifier. Hence, this sensor cannot be trusted for the data with the engine loaded, and is also suspect for the earlier, unloaded data, although there is no explicit evidence of time dependence in its sensitivity for the earlier data. A 2.5% change in the calibration constant of this transducer would move the 3rd-stage experimental point in Fig. 5(b) into perfect agreement with the calculation, without changing the other two experimental points in Fig. 5(b).

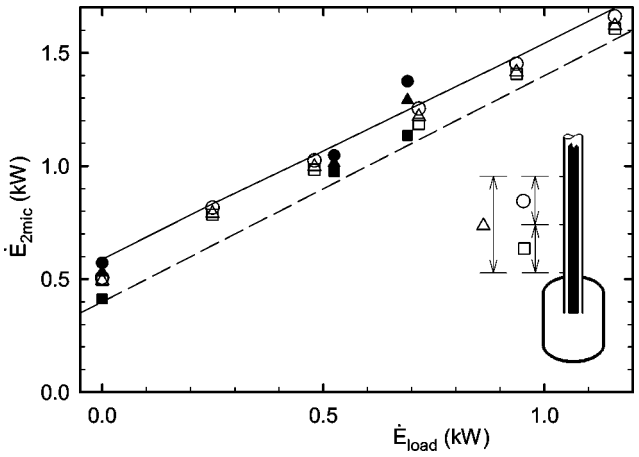

FIG. 6. Acoustic power $\dot{E}_{2\mathrm{mic}}$ flowing down the lower resonator pipe as a function of acoustic power $\dot{E}_{\mathrm{load}}$ dissipated in the loads, with pressure amplitudes of 242–252 kPa between the 1st and 2nd stages. The open symbols represent measurements with the RC loads and with the fan cooling the lower compliance. The filled symbols are measurements under other circumstances, as described in the text. The inset shows which symbols are associated with which pair of pressure transducers for $\dot{E}_{2\mathrm{mic}}$. The dashed line, a guide to the eye, has a slope of unity and an arbitrary vertical offset. The solid line links DeltaE results corresponding to each of the open triangles, with a minor-loss coefficient of 0.7 as described in the text.

Despite this uncertainty about one pressure transducer, the overall evidence for our understanding of the pressure and volume-velocity phasors in this apparatus is very good.

VI. POWERS

The series of three pressure transducers in the lower resonator pipe give three ''pairs'' for three measurements[36] of acoustic power $\dot{E}_{2\mathrm{mic}}$ flowing past this location. Figure 6 shows a comparison of these measurements with the power dissipated below this location. The circles, squares, and triangles indicate which pair of the three transducers is used to obtain $\dot{E}_{2\mathrm{mic}}$, as illustrated in the inset. The horizontal axis is the power $\dot{E}_{\mathrm{load}}$ dissipated in the RC or LC loads, obtained as described in Sec. IV from measured complex pressures in the bottom compliance and the load compliances, and the geometry of the loads (most importantly the volumes of the load compliances). The open symbols represent measurements with 0, 1, 2, 3, 4, and 5 RC loads, and with the fan cooling the lower compliance. The filled symbols near $\dot{E}_{\mathrm{load}}=0.7$ kW represent measurements with the LC load and with the fan cooling the lower compliance. The filled symbols near 0.0 and 0.5 kW represent measurements with 0 and 2 RC loads, respectively, without the fan cooling.

The overall slope near unity displayed by the measurements inspires confidence in both $\dot{E}_{\mathrm{load}}$ and $\dot{E}_{2\mathrm{mic}}$. The slight

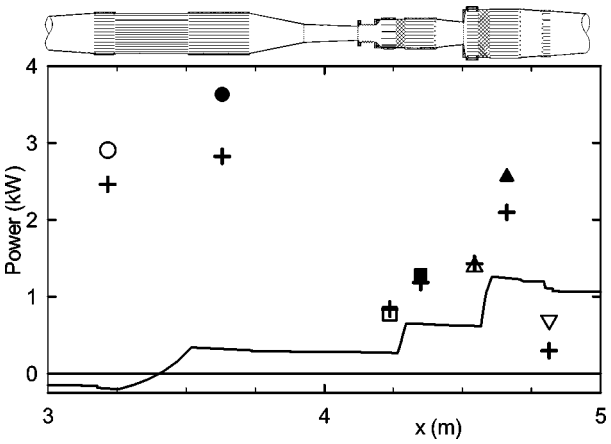

FIG. 7. Powers as a function of position through the three stages, at the same operating point as for Figs. 4 and 5. The solid curve is the calculated acoustic power $\dot{E}$. The symbols are thermal powers at the heat exchangers; on the plot, each symbol is placed horizontally at the center of its heat exchanger. The three filled symbols are experimental hot powers, and the four open symbols are experimental ambient powers. Plus signs are the corresponding calculated thermal powers.

deviation from unity slope shared by the open-symbol measurements and the solid calculated line is due to slightly reduced $|p_1|$ and $|U_1|$ throughout the lower resonator as more power is drawn through the 3rd stage. Of the vertical offset of 0.5 kW in the open-symbol measurements and almost 0.6 kW in the calculated line, 25% is due to dissipation between the sensors and the bottom of the tube and 75% is due to the minor loss at the abrupt transition between the bottom of the tube and the bottom compliance. (We chose to retain the *a priori* estimated value of the minor-loss coefficient, $K=0.7$, in all calculations reported in this paper, instead of changing to $K=0.65$, which would be more compatible with the data in Fig. 6, because we did not want to introduce *any* fitting parameters into the calculations.) The self consistency in Fig. 6 adds to our confidence in the DeltaE modeling of the apparatus.

The three sets of filled symbols in Fig. 6 have a greater vertical spread than do the open symbols. A greater vertical spread seems to indicate a greater dissipation of acoustic power in the resonator pipe between the transducers, yet there is no reason to expect such additional dissipation. Hence, we take this spread as strong evidence that the theory of the measurement[36] of $\dot{E}_{2\mathrm{mic}}$ is not perfectly applicable here. That theory is based on a laminar analysis, but the flow here is turbulent, with a Reynolds-number amplitude of 2×10^6. The increased vertical spread indicates that, at least for turbulent flow, effects not included in the present theory of the measurement should be added. Candidates include an axial temperature gradient in the measurement zone, which was larger when the fan was absent, and an unforeseen sensitivity to the phase of the acoustic impedance, which changes dramatically when substituting one LC load for three RC loads.

Figure 7 displays powers for the same typical operating point as has been described with Figs. 4 and 5. The features shown in Fig. 7 are typical of all data sets. The measured hot powers, indicated by three filled symbols, are simply the electrical powers delivered to the heaters. The measured ambient heat-removal powers, indicated by four open symbols, are the product of the measured water flow rates, the measured temperature differences between inflowing and outflowing water streams, and the density and specific heat of water. The calculated $\dot{E}$ represented by the solid curve and the calculated thermal powers represented by $+$'s are results of the same DeltaE calculation that produced the calculated results in Figs. 4 and 5. The acoustic power is obtained straightforwardly from the calculated phasors, as $\dot{E}=\frac{1}{2}\mathrm{Re}[p_1\tilde{U}_1]$. The calculated thermal powers include the effects of thermoacoustic heat transport through the regenerators and stack, boundary-layer heat transport at the surfaces of the thermal buffer tubes, and ordinary axial conduction in the argon gas and stainless steel through these components. In addition to these standard thermoacoustic heat effects, the DeltaE calculation includes the conduction of heat through the metal shells around the stack, regenerators, and thermal buffer tubes. Estimates of black-body radiation heat transport in the thermal buffer tubes and of heat transport via conduction and convection in the pressurized fiber-packed insulation space around the stages, based on measurements as described in Sec. IV, were added to the DeltaE results. No estimates of Rayleigh streaming and jet-driven streaming in the thermal buffer tubes or internal streaming in the stack and regenerators were included in the calculations.

In Fig. 7, $\dot{E}$ is negative above the 1st stage, showing the delivery of acoustic power from the 1st stage to the unavoidable dissipation in the upper part of the resonator. Here, about a third of the acoustic power produced in the 1st stage is spent in the upper resonator, but this fraction is smaller for other data sets having RC loads in use at the bottom of the resonator. Acoustic power from the 1st stage is more than doubled in the 2nd stage, and then redoubled in the 3rd stage. Dissipation in the hot heat exchanger and flow straighteners below the 3rd stage is larger than for the 2nd stage, because in the 3rd stage these components are farther from the sweet spot and so they experience higher velocities.

The thermal powers in Fig. 7 display interesting features, in common with all other data sets. The 3rd-stage ambient power and both 2nd-stage powers are in excellent agreement with calculations. Similar measurements and calculations in another traveling-wave engine[17] and in the late-20th-century experience with Stirling engines[38] are also in good agreement, so this is to be expected. However, the 3rd-stage hot power exceeds the corresponding calculation significantly, by about the same amount that the final ambient heat exchanger's power exceeds its calculation. This strongly suggests a common cause for both disagreements: streaming in the 3rd-stage thermal buffer tube, carrying heat from the 3rd-stage hot heat exchanger to the final ambient heat exchanger. This thermal buffer tube has an aspect ratio (diameter/length) of 2.2, while that of the 2nd stage is only 0.9 and those of the 1st stage and nearly all previous thermal buffer tubes and pulse tubes[39] are much smaller. The 1st-stage thermal powers are also significantly higher than the corresponding calculations. The disagreement is comparable to that seen in other standing-wave engines near 10%

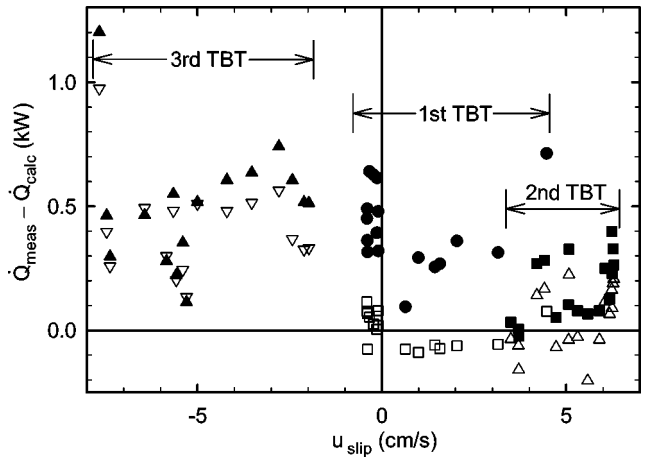

FIG. 8. The difference between the measured and calculated thermal powers associated with each thermal buffer tube, as a function of the calculated effective Rayleigh-streaming slip velocity near the wall of the thermal buffer tube midway along its length. Filled symbols represent power flowing from hot heat exchangers into thermal buffer tubes, and open symbols represent power flowing from thermal buffer tubes into ambient heat exchangers.

amplitude[13,26] and, hence, is not surprising. The observation that the extra 1st-stage hot power exceeds the extra 1st-stage ambient power by a few hundred Watts is initially disturbing—no extra power appears at the neighboring 2nd-stage ambient heat exchanger, so it seems that energy conservation is not obeyed. We suspect that extra heat leak from the 1st-stage hot heat exchanger to the room accounts for these few hundred Watts. An estimation of the correct heat leak to use for the 1st stage based on heat-leak measurements was difficult, because the enormous convective heat transport through the stack at high mean pressure masked heat leak carried from the hot heat exchanger to the pressure-vessel shell by the slow convection in the insulation space. Additionally, during heat leak measurements the hot cone below the hot heat exchanger shared the hot heat exchanger's temperature only at its upper edge, the rest developing a temperature distribution determined by conduction, while during operation the hot cone was kept uniformly hot by vigorous gas motion and, in fact, was hotter than the hot heat exchanger by typically 50 °C, the adiabatic oscillatory temperature amplitude, an effect that has been reported before.[13] Hence, with more hot metal surface area against the insulation space, the 1st-stage hot heat leak to the room should indeed be higher during engine operation than during the heat leak measurements whose results are included in the calculation shown in Fig. 7.

To try to better understand the large heat transport down the 3rd-stage thermal buffer tube, in Fig. 8 we display the excess thermal power, i.e., the difference between measured and calculated thermal powers, for the six heat exchangers abutting the three thermal buffer tubes. For the 1st-stage hot heat exchanger, we have subtracted the excess power in the 1st-stage ambient heat exchanger, because this excess power flows through the stack, not through the thermal buffer tube, as is explained in the previous paragraph. In the 2nd- and 3rd-stage thermal buffer tubes, there is a good correlation between the hot and ambient powers, while in the 1st-stage thermal buffer tube the hot power usually exceeds the ambient power by a few hundred Watts, which we ascribe to increased heat leak, as discussed in the previous paragraph. Overall, except for a few outlying points, around 500 W flows down the 3rd-stage thermal buffer tube, while the 1st- and 2nd-stage thermal buffer tubes carry between zero and a few hundred Watts (and the 1st-stage hot heat exchanger shows a few hundred additional Watts of heat leak).

The horizontal axis in Fig. 8 is the effective slip velocity $u_{\mathrm{slip}}=\dot{m}_{2,w}/\rho_m$ just outside the boundary-layer against the wall of the thermal buffer tube, at the axial center of the thermal buffer tube, calculated using the modified Rayleigh-streaming expression[31] for the streaming mass flux density $\dot{m}_{2,w}$ near the wall. Originally, the tapers of the three thermal buffer tubes were designed to make $u_{\mathrm{slip}}=0$ at 10% amplitude and full load, with the recognition that u_{slip} would be nonzero for other amplitudes or loads. Then we might have hoped to see data for each thermal buffer tube fall on a big "V" with its tip at the origin in Fig. 8, because streaming-driven heat transport down a thermal buffer tube might be roughly proportional to $\rho_m c_p|u_{\mathrm{slip}}|(T_{\mathrm{hot}}-T_{\mathrm{ambient}})$, where c_p is isobaric heat capacity per unit mass, over some range of u_{slip}. A little experimental evidence for such a minimum has been previously reported.[31,40] The 1st stage, for which data fall on both sides of $u_{\mathrm{slip}}=0$, shows only a slight suggestion of such a "V" shape, asymmetrical at best. Unfortunately, the use of the lower-resonator pencil to partly "fix" the design error in the bottom-compliance volume made the acoustic conditions in the other two stages so far from the original design conditions that they do not operate near $u_{\mathrm{slip}}=0$ for any of the data sets. It is unclear how far from $u_{\mathrm{slip}}=0$ the analysis of Ref. 31 should be applicable; perhaps the 2nd- and 3rd-stage thermal buffer tubes' data fall outside this range.

To summarize the thermal aspects of the present experiment, Fig. 9 shows the seven thermal powers and the three hot temperatures as functions of acoustic power flow past the $\dot{E}_{2\mathrm{mic}}$ measurement location near the bottom of the resonator, at full amplitude.

The thermal powers in Fig. 9(a) display the features already discussed above: The 1st-stage measured powers exceed the calculations, as for previous standing-wave engines, with some of the disagreement in the hot power probably due to heat leak to the room. The measured 3rd-stage hot power and the final ambient power exceed their calculated values by equal amounts, presumably due to heat transport down the 3rd-stage thermal buffer tube. The other measured powers are in better agreement with their calculated values.

The measured temperatures in Fig. 9(b) show the same increase with $\dot{E}$ as the calculated T_{metal} shows, but fall about 60 °C below the calculation, in the vicinity of the calculated values of gas temperature. An error in the temperature calculation of this magnitude is not surprising, given the laminar nature of DeltaE's heat-exchanger algorithms and the highly turbulent flow in the apparatus. For these data sets, the DeltaE algorithms yield typically 50 °C gas-to-metal temperature differences in both ambient and hot heat exchangers, so if these calculated differences were instead about 30 °C then the calculations would agree with the measurements. In addition, the drilled stainless-steel hot heat exchanger bodies

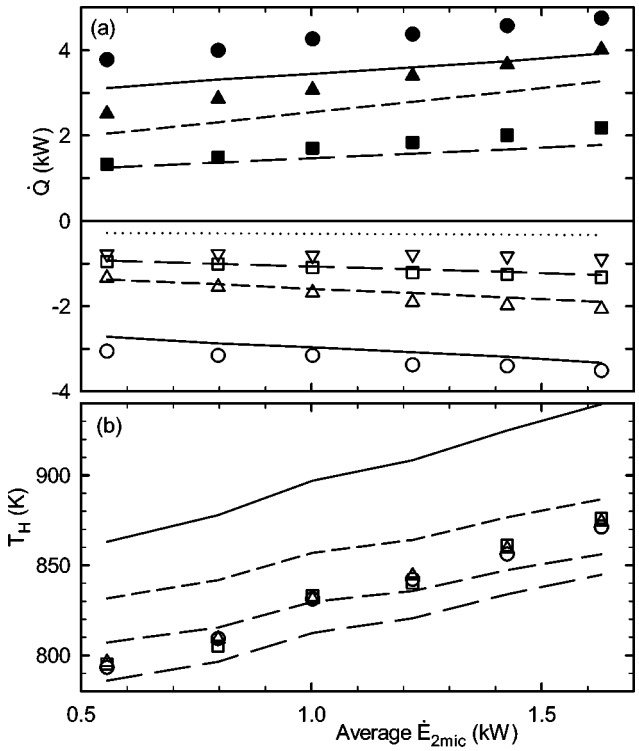

FIG. 9. (a) Thermal powers as a function of load, at full oscillation amplitude. Filled symbols are measured hot powers, and open symbols are measured ambient powers. The lines represent associated calculated values. Circles and solid curves, 1st stage; squares and long-dashed curves, 2nd stage; erect triangles and short-dashed curves, 3rd stage; inverted triangles and dotted curve, final ambient heat exchanger. The sign convention for the ambient powers here is opposite to that used in Figs. 7 and 8, to avoid clutter. (b) Hot temperatures as a function of load, at full oscillation amplitude. Symbols are measured metal temperatures. The solid curve is the calculated metal temperature, forced to be the same for all three stages. The dashed curves are calculated gas temperatures. Circles and long dashes are 1st stage, squares and middle dashes are 2nd stage, and triangles and short dashes are 3rd stage.

are not spatially isothermal. In each heat exchanger, the heaters of various lengths have various powers per unit length, and variations in the number of argon channels close to a unit length of each heater also exist. Because stainless steel has a poor thermal conductivity, spatial nonuniformity of as little as 10% in hot power density can cause spatial nonuniformity of 50 °C in the temperature in the larger (1st- and 3rd-stage) hot heat exchangers.

VII. EFFICIENCY

To discuss the efficiency of this engine, we rely mostly on measurements but also slightly on calculations. We define the efficiency to be the ratio of the acoustic power delivered below the final ambient heat exchanger to the sum of the measured electric powers supplied to the three hot heat exchangers. We choose that location to account for the acoustic power because it is where an alternator could be in a heat-driven electricity-generating system and it is equivalent to where acoustic power was benchmarked in a previous, exemplary thermoacoustic-Stirling engine.[17] Anticipating this choice, we designed the present apparatus for minimum height—not maximum efficiency—below this location. The two-microphone measurements of acoustic power were made 2 m below this location, but we are confident in the ability of the computer model of the apparatus to account for the difference in $\dot{E}$ between these two locations. To define a Carnot efficiency $1-T_{\text{ambient}}/T_{\text{hot}}$ with which to compare the engine's efficiency, we use the incoming water-stream temperature as T_{ambient} and the average of the three measured hot temperatures as T_{hot}.

The efficiencies of the operating points shown in Fig. 9 were, from left to right, 0.15, 0.16, 0.17, 0.18, 0.19, and 0.20. At this fixed amplitude of 10%, efficiency rises as delivered power increases because the deliberate load applied at the bottom of the engine becomes a larger fraction of the total acoustic power that the three stages create, and also the thermodynamically useful heat consumed by the three stages dominates their heat leaks more strongly. Another interesting operating point, not shown in Fig. 9, had all five RC loads open and an amplitude of only 8.5%, yielding an efficiency of 0.18. At this lower-power operating point, the heat leaks were a larger fraction of the delivered hot powers, but this was mostly compensated by lower dissipation of acoustic power in the upper resonator and the regenerators, where the dissipation is more nearly proportional to the cube of the amplitude than to its square.

A more detailed analysis of the sources of dissipation in the engine is conveniently made in terms of exergy, the thermodynamic energy (or, here, power) that accounts for the ability to do useful work.[41] The exergy power associated with acoustic power in open space equals the acoustic power itself, but the exergy power of acoustic power in a porous medium is more complicated.[42] The exergy power associated with a heat source $\dot{Q}$ at temperature T is

$$\dot{Q}(1-T_{\text{ambient}}/T), \tag{8}$$

where T_{ambient} is the temperature at which heat is freely available in the environment. An analysis of a thermodynamic system in terms of either exergy or irreversible entropy generation allows a quantitative discussion of the irreversibilities in the system by subdividing it into logical sets of processes, locations, etc.[41,43]

At its most efficient operating point, the total exergy input power to the cascade engine via the three hot-heat-exchanger powers, given by Eq. (8), was 7322 W. The acoustic power (and, hence, exergy power) delivered below the final ambient heat exchanger was 2179 W. Hence, 5143 W of exergy power was lost in the conversion of thermal to acoustic power by the engine. Four per cent of that was lost in the upper resonator, 49% in the 1st stage, 18% in the 2nd stage, and 29% in the 3rd stage. That the 3rd stage is responsible for more irreversibility than the 2nd is to be expected, since it is also responsible for more acoustic-power production. That almost half of the irreversibility occurs in the 1st stage, even though it creates less than a third of the acoustic power, is due to the intrinsically irreversible nature of standing-wave thermoacoustics.

The ''Experiment'' column of Table III shows a further subdivision of lost exergy, by location and process, for this most efficient operating point. The largest irreversibility is the sum of the well-understood viscous, thermal-relaxation, and axial conduction phenomena in the stack, effects that are

TABLE III. Rate of exergy loss in the engine at 10% amplitude and full load, subdivided according to location and process, in order of importance. The first column of numbers gives the exergy accounting for the most efficient experimental operating point, the second column shows the improvement possible with circumstances that we are very confident could be achieved with a scaled-up helium engine, and the third column shows the further improvement possible with reasonable probability. HX = heat exchanger; TBT = thermal buffer tube.

	Experiment	Confident future	Probable future
—Lost exergy power:—			
1st stage, stack, known processes	1177 W	14.1 kW	14.1 kW
1st stage, unknown heat	554 W	7.1 kW	7.1 kW
1st stage, dT, ambient HX	532 W	8.5 kW	4.3 kW
3rd stage, unknown heat	496 W	7.9 kW	4.0 kW
3rd stage regen., known processes	309 W	2.3 kW	2.3 kW
2nd stage regen., known processes	294 W	3.3 kW	3.3 kW
2nd stage, unknown heat	266 W	4.3 kW	2.2 kW
3rd stage dT, ambient HX	261 W	4.2 kW	2.1 kW
3rd stage, expt heat leak	230 W	1.8 kW	1.8 kW
3rd stage, TBT, known processes	213 W	2.3 kW	2.3 kW
Upper resonator	192 W	3.1 kW	3.1 kW
2nd stage, expt heat leak	145 W	1.2 kW	1.2 kW
2nd stage, dT, ambient HX	144 W	2.3 kW	1.2 kW
1st stage, expt heat leak, fiber insul.	98 W	7.8 kW	7.8 kW
Sum of smaller effects	234 W	3.2 kW	3.2 kW
Total lost exergy power	5143 W	66.4 kW	52.8 kW
Delivered exergy power	2179 W	34.9 kW	34.9 kW
Percent of Carnot	30%	34%	40%

inherent in standing-wave engines and are included in the DeltaE calculations describing the apparatus. This is a price one chooses to pay in using the cascade arrangement for a thermoacoustic engine. Next largest is the ''extra'' hot power consumed by the 1st stage that can be accounted for neither in the calculations nor by the heat leak measurements. Standing-wave engines near 10% amplitude have always suffered from such extra heat consumption.[13,26] Next in importance in Table III is irreversible heat transfer at the 1st-stage ambient heat exchanger, where a calculation shows that the ambient waste heat of the 1st stage must flow across a difference of 50 °C between the average temperature of the oscillating gas and the metal temperature.

The fourth entry in the table is the thermal power that we suspect is carried by streaming in the 3rd-stage thermal buffer tube, as discussed in the previous section. The fifth and sixth entries are the well-understood lossy processes in the two regenerators, caused by viscosity and imperfect thermal contact. These are large in this cascade arrangement, relative to traditional Stirling engines, because both regenerators are forced significantly away from the sweet spot of small velocity amplitude where the phase difference between pressure and velocity is zero.

The exact values of some of the numbers in this table should not be taken too seriously. The excellent agreement between calculated and measured complex pressures gives us confidence in numbers associated with the wave and the acoustic power, but some heat and temperature effects are less certain. The worst example is the gas-to-metal temperature difference in the 1st-stage ambient heat exchanger, which is calculated with a laminar algorithm in DeltaE and using the calculated heat flow, even though the oscillations in the heat exchanger are turbulent and the experimental heat flow is larger. The corresponding entry in the table might be in error by as much as 50%. Differences between measured and calculated hot temperatures shown in Fig. 9(a) further highlight the uncertainties in our knowledge of heats and temperatures. Nevertheless, the total lost exergy in the table is a number based on measured thermal and acoustic powers, and on the confidently calculated difference between acoustic powers at the 2-microphone location and the final ambient heat exchanger; most of the individual entries in the table are based on measurements or on dependable calculations.

Two decisions made during the design of this engine had a major impact on its efficiency. First, we decided to use a honeycomb stack instead of a parallel-plate stack, because a stainless-steel honeycombs are commercially available. Calculations predict that the honeycomb performs about 20% less efficiently than parallel plates. In one experimental engine in which we used both types of stack (unpublished), the hot power consumed in excess of the calculated amount was also reduced, by at least 20%, by parallel plates instead of honeycomb. Second, we decided to use argon instead of helium in this engine, for reasons described in the Introduction. Thermoacoustically, the present engine is strictly ''similar'' to[26] an engine in which every spatial dimension would be double that of the present engine and which would be filled with 3.1-MPa helium instead of 2.4-MPa argon. However, perfect similitude would also require that the present engine be built of metals with a thermal conductivity 8.5× lower than that of the metals (presumably stainless steel) of the hypothetical helium engine, and that the acceleration of gravity be 5× lower and the insulation fiber sizes in the pressure housing be 2× smaller for the present engine, in order for metallic heat conduction and convection-borne heat leaks to scale correctly. Accounting for these easily calculable thermal effects while otherwise scaling up powers by a factor of 16, and simultaneously incorporating the difference between honeycomb stacks and parallel-plate stacks, yields the numbers in the ''Confident'' column of Table III, showing that a cascade engine of double the present size, filled with helium and of stainless-steel construction, (or, equivalently, one of the present size and argon, but with an imaginary low-conductivity construction material and in reduced gravity) can certainly achieve 34% of Carnot's efficiency.

Other straightforward improvements should raise the efficiency further. Smaller passages in the heat exchangers would reduce the exergy wasted in the temperature defects in them. Reducing these passage sizes by a factor of two might reduce these losses by a similar factor. Avoiding the mistake in the design of the resonator, which put the 2nd- and especially 3rd-stage thermal buffer tubes far from zero Rayleigh streaming in the present engine, would presumably reduce the heat transported by streaming in these two thermal buffer tubes significantly, perhaps by about a factor of 2. Accounting for these two improvements yields the ''Probable'' column in Table III, showing that the efficiency of a cascade engine can probably reach 40% of Carnot's efficiency, the same as that of the most efficient thermoacoustic-Stirling engine built to date.[17]

Whether the cascade configuration is superior for any actual applications will depend on practical issues, such as the cost of construction, that are beyond the scope of the present paper.

ACKNOWLEDGMENTS

We are grateful to Chris Espinoza, Mike Torrez, Brad Sims, and Bob Miller for attention to detail paid during the construction of this apparatus, to Scott Backhaus for helpful discussions during the analysis of the data, and to John Wollan for a careful reading of the manuscript. This work was supported by OBES/DMS in the U.S. Department of Energy's Office of Science, and by Praxair, Inc.

[1] Lord Rayleigh, ''The explanation of certain acoustical phenomena,'' Nature (London) **18**, 319–321 (1878).
[2] W. A. Marrison, ''Heat-controlled acoustic wave system,'' U.S. Patent No. 2,836,033, 1958.
[3] R. L. Carter, M. White, and A. M. Steele (private communication of Atomics International Division of North American Aviation Inc., 1962). See also K. T. Feldman, ''A study of heat generated pressure oscillations in a closed end pipe,'' Ph.D. dissertation, Mechanical Engineering Department, University of Missouri, 1966.
[4] K. T. Feldman, ''Review of the literature on Sondhauss thermoacoustic phenomena,'' J. Sound Vib. **7**, 71–82 (1968), and hard-to-find references therein.
[5] P. H. Ceperley, ''A pistonless Stirling engine—The traveling wave heat engine,'' J. Acoust. Soc. Am. **66**, 1508–1513 (1979).
[6] P. H. Ceperley, ''Gain and efficiency of a short traveling wave heat engine,'' J. Acoust. Soc. Am. **77**, 1239–1244 (1985).
[7] R. S. Wakeland and R. M. Keolian, ''Thermoacoustics with idealized heat exchangers and no stack,'' J. Acoust. Soc. Am. **111**, 2654–2664 (2002).
[8] G. Walker, *Stirling Engines* (Clarendon, Oxford, 1960).
[9] N. Rott, ''Damped and thermally driven acoustic oscillations in wide and narrow tubes,'' Z. Angew. Math. Phys. **20**, 230–243 (1969).
[10] N. Rott, ''Thermally driven acoustic oscillations, part III: Second-order heat flux,'' Z. Angew. Math. Phys. **26**, 43–49 (1975).
[11] N. Rott, ''Thermoacoustics,'' Adv. Appl. Mech. **20**, 135–175 (1980).
[12] A. Migliori and G. W. Swift, ''Liquid sodium thermoacoustic engine,'' Appl. Phys. Lett. **53**, 355–357 (1988).
[13] G. W. Swift, ''Analysis and performance of a large thermoacoustic engine,'' J. Acoust. Soc. Am. **92**, 1551–1563 (1992).
[14] T. J. Hofler and M. S. Reed, ''Measurements with wire mesh stacks in thermoacoustic prime movers,'' J. Acoust. Soc. Am. **99**, 2559–2574 (1996).
[15] J. A. Lightfoot, W. P. Arnott, H. E. Bass, and R. Raspet, ''Experimental study of a radial mode thermoacoustic prime mover,'' J. Acoust. Soc. Am. **105**, 2652–2662 (1999).
[16] T. Yazaki, A. Iwata, T. Maekawa, and A. Tominaga, ''Traveling wave thermoacoustic engine in a looped tube,'' Phys. Rev. Lett. **81**, 3128–3131 (1998).
[17] S. Backhaus and G. W. Swift, ''A thermoacoustic-Stirling heat engine: Detailed study,'' J. Acoust. Soc. Am. **107**, 3148–3166 (2000).
[18] C. M. de Blok, ''Thermoacoustic system, 1998,'' Dutch Patent: International Application Number PCT/NL98/00515, U.S. Patent 6,314,740, November 13, 2001.
[19] G. W. Swift, *Thermoacoustics: A Unifying Perspective For Some Engines and Refrigerators* (Acoustical Society of America Publications, Sewickley, PA, 2002).
[20] T. J. Hofler, ''High-efficiency heat-driven acoustic cooling engine with no moving parts, '' U.S. Patent No. 5,901,556, 1999.
[21] A. J. Lesperance, ''Hardware modifications and instrumentation of the thermoacoustically driven thermoacoustic refrigerator,'' Master's thesis, U.S. Naval Postgraduate School, Monterey, CA, 1997.
[22] S. Backhaus and G. W. Swift, ''Fabrication and use of parallel-plate regenerators in thermoacoustic engines,'' in *Proceedings of the 36th Intersociety Energy Conversion Engineering Conference* (American Society of Mechanical Engineers, New York, NY, 2001), pp. 453–458.
[23] G. Petculescu and L. A. Wilen, ''Traveling-wave amplification in a variable standing wave ratio device,'' Acoustic Research Letters Online **3**, 71–76 (2002).
[24] D. Gedeon, ''DC gas flows in Stirling and pulse-tube cryocoolers,'' in *Cryocoolers 9*, edited by R. G. Ross (Plenum, New York, 1997), pp. 385–392.
[25] G. W. Swift and J. J. Wollan, ''Thermoacoustics for liquefaction of natural gas,'' GasTIPS **8**(4), 21–26 (2002). Also available at www.lanl.gov/thermoacoustics/Pubs/GasTIPS.pdf.
[26] J. R. Olson and G. W. Swift, ''Similitude in thermoacoustics,'' J. Acoust. Soc. Am. **95**, 1405–1412 (1994).
[27] Ref. 19, Eq. (4.76).
[28] Boiler and Pressure Vessel Committee of the American Society of Mechanical Engineers, *ASME Boiler and Pressure Vessel Code* (American Society of Mechanical Engineers, New York, 2001).
[29] Fiberfrax®, Unifrax, Niagara Falls, New York.
[30] Kentucky Metals, New Albany, Indiana.
[31] J. R. Olson and G. W. Swift, ''Acoustic streaming in pulse tube refrigerators: Tapered pulse tubes,'' Cryogenics **37**, 769–776 (1997).
[32] Endevco, San Juan Capistrano, CA.
[33] Ohio Semitronics, Hilliard, OH.
[34] W. C. Ward and G. W. Swift, ''Design environment for low amplitude thermoacoustic engines (DeltaE),'' J. Acoust. Soc. Am. **95**, 3671–3672 (1994). Software and user's guide available either from the Los Alamos thermoacoustics web site at www.lanl.gov/thermoacoustics/ or from the Energy Science and Technology Software Center, U.S. Department of Energy, Oak Ridge, Tennessee.
[35] I. E. Idelchik, *Handbook of Hydraulic Resistance*, 3rd ed. (Begell House, New York, 1994).
[36] A. M. Fusco, W. C. Ward, and G. W. Swift, ''Two-sensor power measurements in lossy ducts,'' J. Acoust. Soc. Am. **91**, 2229–2235 (1992).
[37] Ref. 19, Eq. (4.72).
[38] A good overview of this large body of work can be found in proceedings of the annual Intersociety Energy Conversion Engineering Conferences and the less frequent International Stirling Engine Conferences.
[39] R. Radebaugh, ''A review of pulse tube refrigeration,'' Adv. Cryog. Eng. **35**, 1191–1205 (1990).
[40] G. W. Swift, M. S. Allen, and J. J. Wollan, ''Performance of a tapered pulse tube,'' in *Cryocoolers 10*, edited by R. G. Ross, Jr. (Plenum, New York, 1999).
[41] A. Bejan, *Advanced Engineering Thermodynamics*, 2nd ed. (Wiley, New York, 1997).
[42] Ref. 19, Eq. (6.21).
[43] R. C. Tolman and P. C. Fine, ''On the irreversible production of entropy,'' Rev. Mod. Phys. **20**, 51–77 (1948).